VENUS: A Vertical-Cavity Surface-Emitting Laser Electro-Opto-Thermal NUmerical Simulator

Alberto Tibaldi ⓘ, Francesco Bertazzi ⓘ, Michele Goano ⓘ, *Member, IEEE*,
Rainer Michalzik, and Pierluigi Debernardi

Abstract—**The properties of vertical-cavity surface-emitting lasers (VCSELs) are investigated by means of a multiphysical Vcsel Electro-opto-thermal NUmerical Simulator (VENUS). VENUS includes a three-dimensional vectorial electromagnetic code, a description of the quantum well optical response, a heat equation solver, and a quantum-corrected drift-diffusion simulator. The proposed suite includes coupling mechanisms often overlooked in VCSEL simulation and allows to reassess the impact of parameters, which can be critically dependent on implementation details inaccessible in commercial codes. The agreement with experimental results holds the promise of the application of this framework to the computer-aided design of innovative VCSEL concepts.**

Index Terms—**VCSELs, multiphysical simulation, drift-diffusion, electrothermal, optical VCSEL modes.**

I. INTRODUCTION

VERTICAL-CAVITY surface-emitting lasers (VCSELs) are currently experiencing their best time so far. After becoming undisputed leaders in datacom and sensing contexts [1], they are now invading the smartphone and automotive markets as key elements in a plethora of cutting-edge innovations; two remarkable examples are the dot projector adopted in the Apple TrueDepth technology and the LiDAR for self-driving cars [2], [3]. The VCSELs' success is due to their low energy consumption, low cost, on-chip testability, and the natural possibility to build arrays. In order to export these advantages to the widest range of upcoming applications, the VCSEL community is exploring novel concepts and materials, aiming to achieve wavelength-tunable devices [4], [5] and/or to move towards mid-infrared [6], [7] or blue [8] wavelengths. Facing the challenges of this upcoming human-laser interaction era will require new reliable and optimized VCSEL designs. For this reason, computer-aided design (CAD) tools will play a major role as supporting prototyping frameworks, to replace expensive trial-and-error manufacturing campaigns.

While from the optical point of view a VCSEL can be described as an open dielectric resonator, from the electrical standpoint it is basically a complicated *pin* diode. Still, neither description considered individually is sufficient to describe the VCSEL lasing operation, which results from the interplay of these physics. Moreover, VCSEL designs are not material- or application-agnostic. Considering for example the forthcoming GaN-based VCSELs, limiting the analysis to the mere determination of its optical modes would neglect all the carrier transport issues constituting the stumbling blocks in their design. On the other hand, an analysis limited to carrier transport would provide no information about lasing action and emitted beam. In addition to optics and electronics, also thermal features play a major role, being the cause of the roll-over phenomenon that limits the maximum optical power. To summarize, a realistic VCSEL simulator must describe the coupling of carrier transport, heating and optical mode properties.

Over the last 20 years, many researchers have developed multiphysical VCSEL models: after the seminal work of Hadley *et al.,* [9], noteworthy models have been proposed by groups from Hagen [10], Chalmers [11], Budapest [12], IEIIT-CNR [13] and Lodz [14]. All these works are based on phenomenological carrier rate equations; in fact, to the best of our knowledge, the first physics-oriented comprehensive VCSEL simulators were proposed by Streiff *et al.* of the ETH Zurich Optoelectronics Group [15] and by Mehta *et al.* [16]. Streiff's work was later introduced in the commercial simulator ISE TCAD [17], but it is currently no longer supported nor documented [18]. Other commercial modeling suites that can be used for VCSEL simulation include PICS3D [19] from Crosslight Software and LaserMOD [20] from Synopsys RSoft, which currently do not manage vectorial modes and therefore cannot be used to design polarization-stable VCSELs.

In an effort to advance in this field and fill the present lack of established VCSEL CAD tools, in this work we present our in-house developed Vertical-cavity surface-emitting laser Electro-opto-thermal NUmerical Simulator (VENUS). Section II describes the VENUS constituents and their coupling strategy.
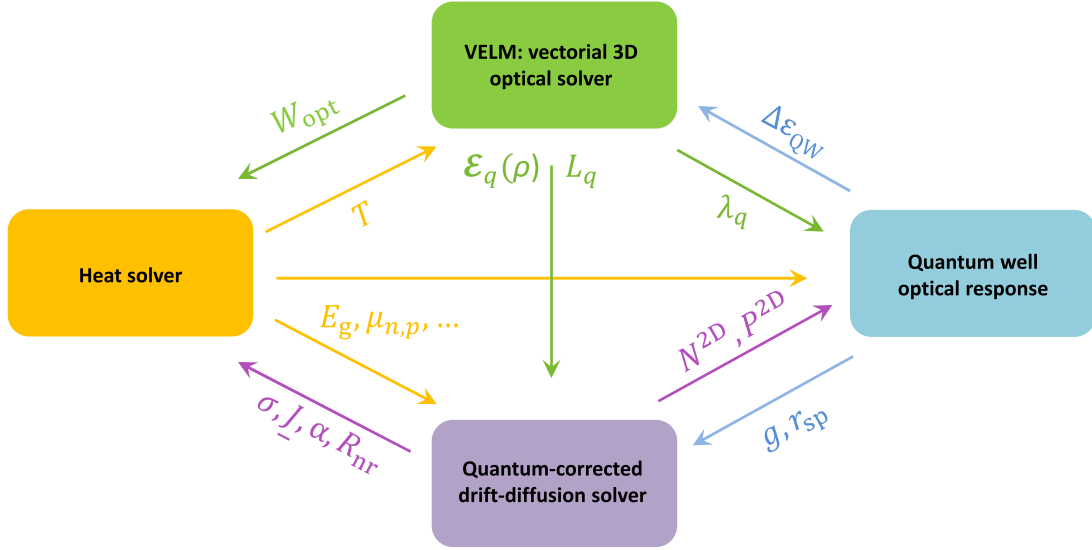
Fig. 1.   Schematic representation of the constitutive blocks of VENUS and of their interplay. Each block is described in the corresponding section.

Similarly to [15], carrier transport is described by a drift-diffusion model including quantum corrections for the active region. The optical mode solver is our efficient 3D vectorial Vcsel ELectroMagnetic code VELM [21], [22]. A fast and accurate thermal simulator based on the mortar element method (MEM) has been developed, which exploits multi-domain spectral elements as a very natural choice to represent heating phenomena. The calibration and validation of VENUS through comparisons with experimental results [23] are reported in Section III. Particular attention is dedicated to the thermal roll-over, which is a crucial phenomenon in VCSEL operation, as it sets the maximum available optical power. This is the most complex phenomenon to be correctly reproduced, because it is ruled by the complex temperature dependence of the different recombination terms, Auger in particular. The role of the different effects is discussed.

II. VENUS CONSTITUTIVE BLOCKS

A schematic overview of this Section is reported in Fig. 1. The VENUS constitutive blocks and their interplay are described in detail in the following subsections.

A. VELM: Vectorial 3D Optical Solver

From the electromagnetic point of view, a VCSEL is an open dielectric resonator. The operation wavelength is defined by its resonance condition, and lasing occurs when active carriers induce a gain profile that compensates material and radiation losses. For this reason the main outputs of a VCSEL optical simulator are the modal losses L_q, in addition to the q-th mode field profile $\mathcal{E}_q$ and its wavelength λ_q.

VCSELs are very complex structures, composed of hundreds of layers and related details. Among the techniques proposed to solve the VCSEL optical problem are scalar approaches, such as the effective index method [9], and full-wave schemes. These include both fully numerical methods and semi-analytical tech-

niques, which exploit geometrical symmetries such as the longitudinal invariance to reduce the computational cost [24]. A remarkable example of the fully numerical class is the frequency-domain finite element (FE) solver LUMI, which uses a 2D body-of-revolution expansion for axisymmetric devices and perfectly matched layer boundary conditions [15]. An example belonging to the semi-analytical class is the method of lines (MoL), which adopts a spatial discretization in the radial direction and a transmission line formalism in the longitudinal direction [10]. Other noteworthy examples of semi-analytical techniques rely on plane-wave expansions, where, just like in MoL, the field is propagated along the longitudinal direction by admittance [25] or reflection matrix [26] formulations.

In this work we use our VELM code [21], [22] as optical mode solver. This is based on representing the electromagnetic field in terms of the modal basis $\{\mathbf{E}_\mu\}$ of a reference medium in cylindrical coordinates (Bessel functions of the first kind)

$$\mathcal{E}(\rho, \varphi, z) = \sum_\mu \int A_\mu(z, k)\, \mathbf{E}_\mu(\rho, \varphi, k)\, \mathrm{d}k, \qquad (1)$$

where k is the transverse wavevector and $\mathbf{A} = \{A_\mu\}$ is the vector of the unknown mode amplitudes. The index μ spans forward and backward propagation, field polarization (TE and TM) and azimuthal mode variations, so that VELM is a full-wave vectorial 3D model.

All the deviations with respect to a reference medium are described by coupled-mode theory. The field expansion coefficients in a longitudinally invariant section obey

$$\frac{\mathrm{d}\mathbf{A}}{\mathrm{d}z} = (\mathbf{B} + K_{\mu\mu'}\Delta k)\mathbf{A}, \qquad (2)$$

where $\mathbf{B} = \mathrm{diag}\{-\mathrm{j}\beta_\mu\}$ is the diagonal matrix of propagation constants in the reference medium, $\mathrm{j} = \sqrt{-1}$ is the imaginary unit. The coupling coefficients $K_{\mu\mu'}$, expressed as transverse integrals of Bessel functions over the area S of the computation window, can be decomposed into their transverse and

longitudinal contributions

$$(K_{\mathrm{t}})_{\mu\mu'} = -\frac{\mathrm{j}\omega}{C_\mu} \int_S \mathbf{E}_{\mathrm{t},\mu} \cdot \mathbf{E}_{\mathrm{t},\mu'} \underline{\underline{\Delta\varepsilon_{\mathrm{t}}}} \, \mathrm{d}S \qquad (3)$$

$$(K_z)_{\mu\mu'} = -\frac{\mathrm{j}\omega}{C_\mu} \int_S E_{z,\mu} \cdot E_{z,\mu'} \frac{\varepsilon_{\mathrm{r}}\Delta\varepsilon_z}{\varepsilon_{\mathrm{r}} + \Delta\varepsilon_z} \, \mathrm{d}S, \qquad (4)$$

where C_μ is a normalization constant and $\underline{\underline{\Delta\varepsilon_{\mathrm{t}}}}$ and $\Delta\varepsilon_z$ are the transverse and longitudinal components of the tensor of the deviations from the reference permittivity. The solution of (2) can be expressed in the form of an exponential matrix, hence the mode amplitudes at the two interfaces of each layer with thickness l_ℓ can be related by

$$\mathbf{A}(z_{\ell+1}) = \exp\left[(\mathbf{B} + \mathbf{K}_\ell)l_\ell\right] \mathbf{A}(z_\ell) = \mathbf{T}_\ell \mathbf{A}(z_\ell), \qquad (5)$$

where the transmission matrix $\mathbf{T}_\ell$ has been defined. By cascading the transmission matrices of each section of the device one can compute the overall transmission matrix between two boundaries, beyond which the domain is homogeneous. The solution of the problem is obtained by relating backward to forward waves at these two sections. The condition for an electromagnetic field to be a resonance mode is to replicate itself after a full round-trip; this is rephrased into an eigenvalue problem, whose complex eigenvalues represent the modal wavelengths and the corresponding modal losses (real and imaginary parts, respectively), while the eigenvectors represent the field expansion coefficients. This model would be exact if one did not have to discretize the infinite terms in the expansion (1), transforming the integral into a finite sum with Δk weights. In addition to the cold-cavity refractive index profile of the device, this model includes also the index changes induced by thermal and electrical effects, the carrier-induced gain profile and free-carrier absorption by means of the Drude model [27]. All these 2D (QW) and 3D (temperature) effects are included by staircase approximations.

B. Quantum Well Optical Response

The optical response of a semiconductor is essential, for it provides the gain, the spontaneous emission and the carrier-induced refractive index change of the active region.

This task requires the computation of the band structure of the quantum well (QW) active region. In view of obtaining a reasonable accuracy with moderate computational resources, a 4-band $\mathbf{k} \cdot \mathbf{p}$ method has been adopted, which includes electrons, heavy holes, light holes and the split-off band. By discretizing the $\mathbf{k} \cdot \mathbf{p}$ equations along the QW growth direction and using plane waves as basis functions in the transverse direction, an eigenproblem is solved for each transverse electron wavevector $\mathbf{k}$ in order to obtain the QW subbands. The well-known problem of unphysical spurious solutions has been tackled by applying the FE scheme to the formulation proposed in [28], which provides a correct representation of the projections of the differentiation operators [29]. A change of basis is performed to obtain the formulation presented in the appendix of [30], which lends itself to be reduced to 4×4 independent sub-blocks after the application of the axial approximation. Assuming flat bands proves to be adequate in the lasing regime

of GaAs QW-based VCSELs. However, the flexibility of our FEM would allow to simulate more general potential profiles. This is critical for instance in polar semiconductors such as GaN, where strong charge sheets arising at heterointerfaces induce relevant quantum-confined Stark effects [31].

The carrier-induced permittivity change $\Delta\varepsilon_{\mathrm{QW}}$ of a QW can be computed by Fermi's golden rule as the sum of all of its electron/hole subbands l, m [32]–[34]

$$\Delta\varepsilon_{\mathrm{QW}}(n, p, \lambda, T) = \sum_{l,m,\mathbf{k}} |\hat{\mathbf{e}} \cdot \mathbf{M}_{l,m}(\mathbf{k})|^2 \, (f_{\mathrm{c},l} - f_{\mathrm{v},m})\mathcal{L}(\Delta E),$$
$$(6)$$

where $\mathbf{k}$ is the wavevector, the transition dipole matrix element $\mathbf{M}_{l,m}(\mathbf{k})$ can be evaluated from the overlap of the eigenfunctions resulting from the computation of the band structure, and $\Delta E = E_{l,m}(\mathbf{k}) - \hbar\omega$. The permittivity (6) depends on the injected carrier concentrations through the Fermi functions $f_{\mathrm{c},l}$, $f_{\mathrm{v},m}$, on the wavelength through the photon energy $\hbar\omega$, and on the temperature through $f_{\mathrm{c},l}$, $f_{\mathrm{v},m}$ and $E_{l,m}$ (see Appendix A).

The gain g and the carrier-induced antiguiding Δn are obtained from the imaginary and real part of (6), respectively. A similar expression holds for the spontaneous recombination r_{sp}. The scattering relaxation is included by the lineshape broadening $\mathcal{L}$. After exploring several models proposed in the literature spanning from the classic Lorentzian [33] to more sophisticated models including carrier-carrier effects [35], we decided to include non-Markovian features following the work by Tomita [36], as it provides the best comparison with the experimental laser operation curves.

Many-body effects, with specific reference to the bandgap shrinkage induced by carrier-carrier interactions, have been included as well in the computations [37, App. E], [38].

Since the optical response simulation is computationally demanding, it is evaluated *a priori* on a large parameter space, saved in a 4-D (electron and hole densities, wavelength and temperature) look-up table and interpolated during the multiphysical simulations.

C. Heat Solver

Heating is behind all the phenomena limiting the VCSEL operation, such as the drop of the optical gain and electrical conductivity and the increase of non-radiative recombinations. At steady state, thermal phenomena are described by

$$\nabla \cdot (\kappa \nabla T) = -Q_{\mathrm{tot}}, \qquad (7)$$

where κ is the thermal conductivity and T is the temperature increase referred to the heatsink temperature T_0. The heat sources included in Q_{tot} are the Joule effect, the optical absorption and various non-radiative recombinations:

$$Q_{\mathrm{tot}} = \underbrace{\sigma^{-1} ||\mathbf{J}||^2}_{\text{Joule}} + \underbrace{\alpha W_{\mathrm{opt}}}_{\text{optical}} + \underbrace{E_{\mathrm{g}} R_{\mathrm{nr}}}_{\text{rec.}} + \underbrace{\Delta_{\mathrm{C/V}} C_{n/p}^{\mathrm{cap}}}_{\text{capt./esc.}}. \qquad (8)$$

Here σ is the electrical conductivity computed from the products of carrier density and mobility for electrons and holes, $\mathbf{J}$ is the current density, α accounts for intra-band and free-carrier absorption phenomena distributed according to the 3D
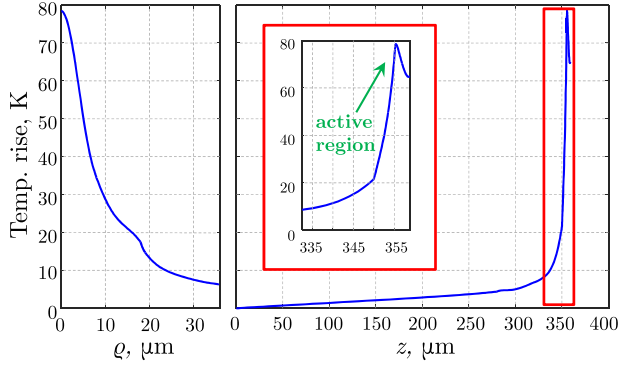
Fig. 2. Typical example of temperature profiles in the device. Left: radial profile at the QW section. Right: longitudinal profile at the device axis, with zoom on the active region where the peak occurs.

modal power density profile W_{opt}, and R_{nr} includes Shockley-Read-Hall (SRH) and Auger recombinations. The contribution of carrier capture/escape is included as the product of conduction/valence band offsets $\Delta_{\text{C/V}}$ and the corresponding capture/escape rates, see eq. (15). Thomson and Peltier effects, not reported in (8), are included in VENUS but result to be negligible compared to the other heat sources.

Figure 2 shows a typical temperature profile. In the right plot reporting the longitudinal temperature profile at the VCSEL axis $\rho = 0$, two regions characterized by different behaviors can be identified: the substrate, where the temperature increase is almost linear, and the active part of the device, where heat is generated and the temperature varies quickly. A very effective numerical scheme in this situation is the mortar element method (MEM) [39], [40]. This is obtained applying the method of weighted residuals to cast (7) in weak form by projecting it on a set of test functions. The projected equations are then transformed into a linear system by expanding temperature as a linear combination of the basis functions. In the widely used Galërkin version, the spaces of basis and test functions are coincident. Compared to FEM, which shares all the aforementioned procedure, MEM uses a low h-refinement scheme. In this way, the domain is decomposed in a small number of sub-domains, exploiting instead a strong p-refinement, based on high-order basis/test functions. This polynomial/Bessel basis is associated to each sub-domain; then, according to mortar-matching, continuity conditions are enforced at the common edges of adjacent sub-domains, achieving a unique set of continuous basis functions. The main advantage of this method is the possibility to define basis functions with different orders in each sub-domain, leading to different spatial resolutions.

The computed 3D temperature profile is used to update all the model temperature-dependent quantities (see Appendix A) and to evaluate the thermal lensing effects by

$$\Delta n(\boldsymbol{\rho}, z) = \frac{\mathrm{d}n}{\mathrm{d}T} T(\boldsymbol{\rho}, z). \qquad (9)$$

D. Quantum-Corrected Drift-Diffusion Solver

The most important section of a VCSEL is the cavity, where the electro-optical interactions producing the stimulated

emission take place. The QW active region is fed by electrons and holes flowing through the surrounding bulk regions, typically the distributed Bragg reflectors (DBRs). Consequently, a CAD-oriented electron transport VCSEL simulation must result from a trade-off between the desired accuracy for the description of quantum regions, and the computational resources required to simulate the whole device. A physics-oriented simulation framework going beyond phenomenological rate equations models [13], but more affordable than genuine quantum models [38], [41] or high-order semiclassical pictures [42], [43] is given by a quantum-corrected drift-diffusion approach [15], [44]–[46]. This is based on separating carriers into two subsets: bulk carriers (n^{3D}, p^{3D}), whose transport is described by the standard drift-diffusion model, and bound carriers (n^{2D}, p^{2D}), which are distributed along the QW confinement direction according to their envelope wavefunctions and can move freely only in the plane parallel to the interfaces. Finally, lasing is described by photon rate equations [13]. The model can be summarized as follows:

$$\begin{cases} -\nabla^2 \phi = \dfrac{q}{\varepsilon}(p^{\text{3D}} - n^{\text{3D}} + p^{\text{2D}} - n^{\text{2D}} + N_{\text{D}}^+ - N_{\text{A}}^-) \\[2mm] \dfrac{\partial n^{\text{3D}}}{\partial t} = \dfrac{1}{q}\nabla \cdot \mathbf{J}_{n^{\text{3D}}} - U_n^{\text{3D}} \\[2mm] \dfrac{\partial p^{\text{3D}}}{\partial t} = -\dfrac{1}{q}\nabla \cdot \mathbf{J}_{p^{\text{3D}}} - U_p^{\text{3D}} \\[2mm] \dfrac{\partial N^{\text{2D}}}{\partial t} = \dfrac{1}{q}\nabla \cdot \mathbf{J}_{N^{\text{2D}}} - U_n^{\text{2D}} \\[2mm] \dfrac{\partial P^{\text{2D}}}{\partial t} = -\dfrac{1}{q}\nabla \cdot \mathbf{J}_{P^{\text{2D}}} - U_p^{\text{2D}} \\[2mm] \dfrac{\partial P_{\text{st},q}}{\partial t} = \Gamma_z(G_q - L_q)P_{\text{st},q} + \Gamma_z S_q, \ q = 1,\dots,N_{\text{modes}} \end{cases}$$
$$(10)$$

The unknowns of this system are the electrostatic potential ϕ, the bulk (n^{3D}, p^{3D}) and bound (a N^{2D}, P^{2D} pair for each quantum well) electron and hole densities, and the stimulated powers at the VCSEL output section associated to the q-th VCSEL mode, $P_{\text{st},q}$. The charge density in the Poisson equation includes both bulk and bound carriers, where the latter are rescaled to volume densities via the related eigenfunctions:

$$n^{\text{2D}} = \sum_m N_m^{\text{2D}}(\boldsymbol{\rho}) \left| \Psi_m^{\text{e}}(z) \right|^2, \ p^{\text{2D}} = \sum_m P_m^{\text{2D}}(\boldsymbol{\rho}) \left| \Psi_m^{\text{h}}(z) \right|^2.$$
$$(11)$$

Since the eigenfunctions are normalized, the 2D densities can be written as $N^{\text{2D}} = \sum_m N_m^{\text{2D}}$ and $P^{\text{2D}} = \sum_m P_m^{\text{2D}}$.

In this work we focus exclusively on the static problem, so that all time derivatives are set to zero. Fermi-Dirac statistics are assumed for both bulk and bound carriers. Still, the expressions of the distribution functions for the two populations are rather different, as they involve the Fermi integral of order $\nu = 1/2$ for the former [47], [48], and the sum over the quantum well bound states for the latter [38], [46].

The choice of the doping species is critical for VCSEL design, and it is very important to take into account incomplete

ionization [49], [50] with the correct activation energies ΔE_D, ΔE_A [51].

For both electrons and holes, the current densities can be expressed in terms of their drift and diffusion constituents

$$\mathbf{J}_n = -\mathrm{q}\mu_n n\nabla[\phi + \widetilde{\phi}_n] + \mathrm{q}D_n\nabla n$$
$$\mathbf{J}_p = -\mathrm{q}\mu_p p\nabla[\phi + \widetilde{\phi}_p] - \mathrm{q}D_p\nabla p, \tag{12}$$

where $\mu_{n,p}$ denote the electron and hole mobilities, the diffusion coefficients $D_{n,p}$ are related to $\mu_{n,p}$ by the Einstein relation, and $\widetilde{\phi}_{n,p}$ are spatially varying terms aimed to include the effect of heterointerfaces and of Fermi–Dirac statistics in the carrier continuity equations:

$$\widetilde{\phi}_n = \chi/\mathrm{q} + V_\mathrm{T}\ln N_\mathrm{C} + V_\mathrm{T}\ln\gamma_n \tag{13}$$
$$\widetilde{\phi}_p = E_\mathrm{g}/\mathrm{q} + \chi/\mathrm{q} - V_\mathrm{T}\ln N_\mathrm{V} - V_\mathrm{T}\ln\gamma_p. \tag{14}$$

Here, the energy gap $E_\mathrm{g} = E_\mathrm{C} - E_\mathrm{V}$, the electron affinity χ, the thermal voltage V_T and the effective densities of states N_C, N_V are assumed position-dependent. This is also the case for the factors $\gamma_{n/p}$ (that include the Fermi–Dirac distribution), which are defined as the ratios of the carrier densities computed with Fermi to those with Boltzmann statistics [38].

The most relevant recombination/generation processes describing the annihilation/creation of electron-hole pairs are those assisted by intermediate trap levels in the forbidden band (SRH), by spontaneous or stimulated photons (radiative), or by other carriers (Auger). These phenomena are taken into account by means of net recombination rates $U_{n,p}$, both for bulk and bound carriers. SRH and Auger processes are modeled using the expressions from [38, p. 49]. Spontaneous recombination processes are described with the phenomenological formula $B_\mathrm{rad}n^\mathrm{3D}p^\mathrm{3D}$ for bulk carriers while, for bound carriers, the net spontaneous recombination rate is evaluated from the r_sp spectrum (see Section II-B).

The bound and bulk carriers are separated in energy to prevent double-counting. Indeed, the 2D and 3D carrier densities are obtained by evaluating the Fermi integrals within the QW boundaries and from the QW top, respectively. The bulk and bound continuity equations are coupled by capture terms modeling scattering events between continuum and bound states. For electrons it reads

$$C_n^\mathrm{cap} = \underbrace{\left(1 - \exp\left(\frac{E_{\mathrm{F},n}^\mathrm{2D} - E_{\mathrm{F},n}^\mathrm{3D}}{k_\mathrm{B}T}\right)\right)}_{\text{capture/escape}} \underbrace{\left(1 - \frac{N^\mathrm{2D}}{N_2}\right)}_{\text{states filling}} \underbrace{\frac{n^\mathrm{3D}}{\tau_\mathrm{scat,n}}}_{\text{capture}} \tag{15}$$

and a similar expression holds for holes. Here, $E_{\mathrm{F},n}^\mathrm{3D}$ and $E_{\mathrm{F},n}^\mathrm{2D}$ indicate the bulk and bound quasi-Fermi levels and N_2 is the maximum density that fits into the QW bound states. The scattering time $\tau_\mathrm{scat,n}$ in this capture model is generally used as a fitting parameter; however, its dependence on the bulk and bound carrier densities could be included following [52], [53]. At thermodynamic equilibrium, the 2D and 3D quasi-Fermi levels are equal, so that the net capture is zero. Depending on the injection condition, (15) can describe either capture or escape
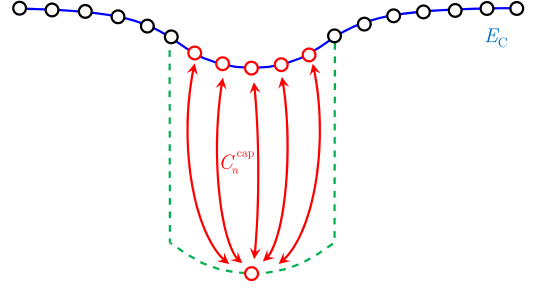

Fig. 3. Graphical description of quantum capture in the conduction band. The red circles indicate the nodes involved in the process. The solid blue and dashed green curves identify the conduction band for bulk and bound carriers.

of bound carriers, as a consequence of $E_{\mathrm{F},n}^\mathrm{3D}$ being below or above $E_{\mathrm{F},n}^\mathrm{2D}$. The "states filling" factor takes into account that the quantum well has a finite number of bound states. This capture term is included with opposite signs in the bulk and bound equations, so that the annihilation of a 3D particle corresponds to the creation of its 2D counterpart, and vice versa. Figure 3 shows a sketch of the 2D – 3D carrier interactions for a one-dimensional mesh: the role of C_n^cap as the connection between the bound and bulk carrier continuity equations is depicted. The energy separation of the 2D and 3D carriers is enforced by evaluating the 3D carrier densities in the QWs by means of Fermi integrals starting from the energy corresponding to the barrier material, thus virtually *hiding* the QW conduction and valence band discontinuities to the bulk continuity equations. Therefore, the solid blue line represents the band structure *experienced* by bulk carriers, while the dashed green line indicates the *actual* conduction band of the QW; more details can be found in [46].

The photon rate equation couples the optical and the electrical blocks. Here, the modal losses L_q and the longitudinal optical confinement factor Γ_z are obtained from the optical solver. The modal gain G_q results from the overlap of the optical field $\mathcal{E}_q$ in the active region with the radial gain profile

$$G_q = \int_0^{2\pi}\int_0^{\rho_\mathrm{max}} g(N^\mathrm{2D}, P^\mathrm{2D}, \lambda_q, T)\,|\mathcal{E}_q(\boldsymbol{\rho})|^2\,\rho\,\mathrm{d}\rho\,\mathrm{d}\varphi, \tag{16}$$

where N^2D, P^2D and temperature vary along the radial direction, and ρ_max is the end of the electrical domain discretization (which could coincide for instance with the radius of the etched mesa in oxide-confined VCSELs). Similarly, S_q is the weighted spontaneous emission, which implicitly includes the spontaneous emission factor, given by

$$S_q = \int_0^{2\pi}\int_0^{\rho_\mathrm{max}} r_\mathrm{sp}(N^\mathrm{2D}, P^\mathrm{2D}, \lambda_q, T)\,|\mathcal{E}_q(\boldsymbol{\rho})|^2\,\rho\,\mathrm{d}\rho\,\mathrm{d}\varphi. \tag{17}$$

In (16) it is assumed that only bound carriers participate in stimulated emission processes. Indeed, transitions associated to bulk carriers would occur at much higher energies, whose corresponding wavelengths are distant from the lasing ones. Therefore, the photon rate equation is coupled only to the continuity equations of bound carriers. This coupling is introduced by the

stimulated recombination term

$$R_{\mathrm{st},q} = \frac{g(N^{2\mathrm{D}}, P^{2\mathrm{D}}, \lambda_q, T)\, |\mathcal{E}_q(\boldsymbol{\rho})|^2}{\int_0^{2\pi} \int_0^{\rho_{\max}} |\mathcal{E}_{\mathrm{out},q}(\boldsymbol{\rho})|^2\, \rho\, \mathrm{d}\rho\, \mathrm{d}\varphi} \frac{P_{\mathrm{st},q}}{\hbar\omega_q}, \qquad (18)$$

where $\mathcal{E}_{\mathrm{out},q}$ is the q-th modal field at the VCSEL output section.

The drift-diffusion equations belong to the class of advection-diffusion problems, so that standard finite difference or finite element schemes would lead to spurious oscillations due to the presence of two competing physical phenomena [54], [55]. Instead, in this work we implemented the standard Scharfetter-Gummel scheme [56], [57], which is a finite-box scheme obtained by assuming a constant current density $\mathbf{J}$ between two nodes i and j having a distance l_{ij}. From this hypothesis it is possible to estimate the electron current flowing through these nodes as

$$\langle \mathbf{J}_n \cdot \widehat{\mathbf{n}} \rangle \simeq \mathrm{q}\frac{D_n}{l_{ij}} \left[n_j \mathcal{B}\left(\frac{\phi_j - \phi_i}{V_{\mathrm{T}}}\right) - n_i \left(\frac{\phi_i - \phi_j}{V_{\mathrm{T}}}\right) \right], \quad (19)$$

where $\mathcal{B}$ indicates the Bernoulli function. A similar expression holds for holes.

III. RESULTS

The structure under study is the AlGaAs surface relief VCSEL described in [23], a λ-cavity device including three QWs and p- (n)-doped DBRs with 24 (38) pairs. Free-carrier absorption is reduced by the modulation doping technique. The contact ring diameter is 16 μm and the structure is considered axisymmetric, with a 6.5 μm oxide aperture. Single-mode emission is achieved by etching a 3 μm-diameter surface relief in the out-coupling facet of the laser [58], thus minimizing losses at the device axis where the fundamental mode has its peak, and suppressing higher-order modes with field distributions away from the relief. As the fundamental mode experiences comparatively higher losses with respect to the standard VCSEL structure, mode competition is effectively prevented at the cost of increasing the threshold current, which in the present case was found to be 3.7 mA, approximately four times higher than the value expected for a multimode VCSEL [23].

Carrier transport and thermal simulations were carried out including the detailed doping and compositional grading profiles of the mirrors layers adjacent to the active region, where carriers may be trapped in high current injection, while a simplified model characterized by an average 44% Al molar fraction was adopted for the DBR structure far away from the active region to reduce the computational burden [15], [59] (this approximation was carefully verified with both 1D and quasi-3D simulations including the full DBR description [59]). The model parameters reported in Appendix A are mostly from the literature when applicable (see references in Table I, except for few parameters that have been fitted to account for the complexity of the structure. For example, the thermal conductivities adopted in this work for the DBR regions differ from the typical (bulk) values by roughly a factor of 2 [60].

The results of the parameter calibration are drawn as red curves in all figures described from now on. A remarkable agreement with all the available experimental data ($V(I)$, $L(I)$,
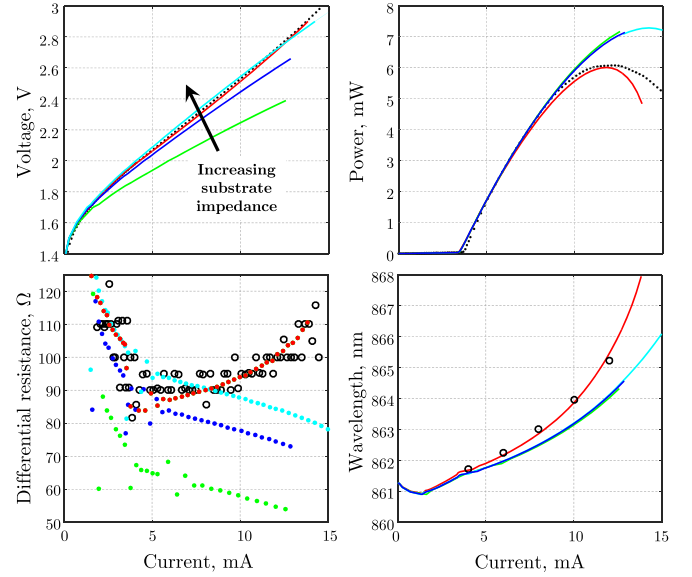

Fig. 4. Results of a simulation campaign performed with VENUS: $V(I)$ curve (top left), $L(I)$ curve (top right), differential resistance (bottom left, open circles indicate experiments), lasing wavelength (bottom right, open circles indicate experiments). Simulations are performed considering the full 350 μm substrate (red), approximating it with a 1 μm thick "substrate" without any correction (green), including a 20 Ω (blue) and 30 Ω (cyan) series resistance. Notice that in the power and wavelength plots the green and blue curves are almost superimposed.

differential resistance and lasing wavelength) was observed in the whole VCSEL operation range, from lasing threshold to roll-over, as it can be seen in Fig. 4. Having validated the model with experimental results and verified its ability to reproduce well-known VCSEL features, we discuss several numerical simulations, which represent an attempt at uncertainty quantification, and also an assessment of the possible impact of simplifying approximations commonly adopted to address the multi-scale and multi-physical problem described by the interplay between the solver blocks shown in Fig. 1. Even though VELM can efficiently handle polarization features, as demonstrated for instance in [61], these are not included here, because measurements are not polarization-resolved.

A. Influence of the Substrate in the Electrical Simulation

In addition to the *reference* results (red lines Fig. 4) obtained including the 350 μm substrate in the electrical simulation region, we also present calculations performed replacing the substrate with a fixed series resistance Z_0, i.e., performing a mixed mode simulation at the carrier transport level. This numerical experiment has been performed for $Z_0 = 0\ \Omega$ (no substrate), 20 Ω and 30 Ω. Setting $Z_0 = 30\ \Omega$ can almost compensate for the absence of the substrate in the $V(I)$ curve, but appreciable discrepancies can be seen in all the other plots, e.g., the VCSEL operation range is overestimated and the wavelength shift is underestimated (black dots and circles indicate experimental results), which can be mainly attributed to the missing heating sources (Joule and non-radiative recombination) in the substrate.
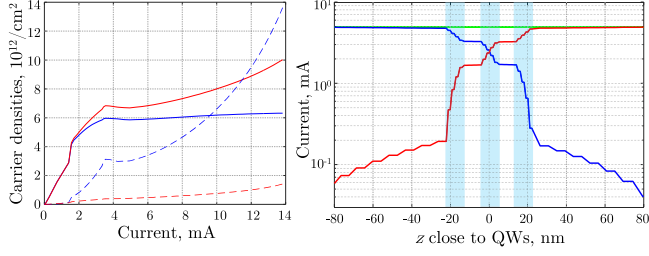
Fig. 5. Left: maximum carrier density over the QW radial section for the reference device simulation. Blue and red curves refer to electrons and holes, respectively. Solid and dashed curves indicate 2D and 3D (multiplied by the QW width) densities, respectively. Right: current profiles in the proximity of the active region, where the QWs are indicated with shadings and $z = 0$ indicates the center of the central QW; the blue and red curves indicate the electron and hole currents. At each longitudinal section, the total current (green curve) is conserved.
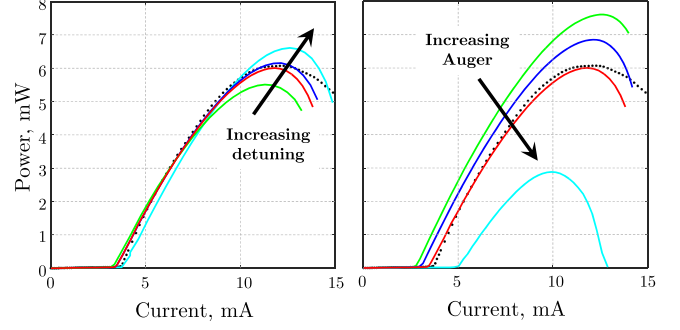

Fig. 6. $L(I)$ characteristics obtained from two parametric simulations. Left: effect of cavity detuning, where the green, blue and cyan simulations refer to $\Delta\lambda = -8$ nm, -5 nm and -2 nm, respectively, and the selected (red) curve is obtained with $\Delta\lambda = -4$ nm. Right: effect of Auger recombination, where the green, blue, red (selected) and cyan curves are obtained with $C_n = C_p = 0.1$, 1, 2.5 and 10×10^{-30} cm^6/ s, respectively.

B. Impact of Auger and Thermal Effects on the Roll-over

Our analysis indicates that the two most relevant causes of the optical power roll-over, the drop of the material gain and Auger recombination, are interrelated. At high injection levels (for the VCSEL under consideration this happens quite soon considering the high threshold current as discussed before), as the temperature increases, more carriers are needed to compensate losses, as required by the photon rate equation (10), which implies $G_m \simeq L_m$ under lasing operation. Eventually, bound electron states are filled first, since P_2 (the maximum bound hole density) is larger than N_2 from (15) by almost a factor of three. In these conditions, only holes can contribute to the gain and the bulk electron population starts increasing. This can be seen in Fig. 5(left), where the 2D (solid curves) and 3D (dashed curves) carrier densities are reported versus current. The lasing threshold is about 4 mA, when 2D electrons (blue) nearly saturate. This gives rise to a much higher corresponding 3D electron density compared to holes (red), which contributes to Auger recombination (with a cubic dependence on carrier density) and other non-radiative recombination channels in the cavity, see the electron and hole contributions of the current density in Fig. 5(right).

The critical parameters in this context are $\Delta\lambda$ and $C_{n/p}^{\mathrm{Aug}}$, whose impacts on the thermal roll-over are shown in Fig. 6 (left and right panels, respectively). The parameter $\Delta\lambda$ is an adjustment of the cavity-gain detuning, which is related to the uncertainty of physical parameters (band-gap or QW composition/thickness/shape/models). Moreover, the devices were grown on wafers characterized by a (almost parabolic) thickness grading from the center to the wafer edge, which introduces an additional thickness uncertainty. The Auger coefficients $C_{n/p}^{\mathrm{Aug}}$ are often treated as fitting parameters in physics-based simulations, because the calculation of phonon-assisted Auger transitions within a full-Brillouin-zone electronic structure framework is currently beyond the grasp of genuine quantum transport models, such as density matrix and the nonequilibrium Green's function approaches. The values adopted here are close to those reported in other VCSEL papers [9], [11], but they are larger by about one order of magnitude compared to other sources [62]. The difference could be ascribed to phonon- and defect-assisted

transitions [63], and possibly to Auger-induced leakage, i.e., the leakage of carriers promoted by Auger recombination to high energies far above the barriers. For example, the inclusion of Auger-induced leakage in drift-diffusion simulations of GaN/InGaN LEDs [64], [65] leads to Auger coefficients compatible with first-principles calculations [66]–[68].

C. Influence of the Oxide Position on the VCSEL Performance

We consider three geometries, corresponding to different positions of the oxide aperture. The oxide aperture is a crucial design feature, whose position was experimentally investigated by the pioneering works in the 1990s, when oxide aperture VCSELs have been proposed. The oxide layer is obtained by growing a thin (about 30 nm-thick) pure AlAs (or AlGaAs with very high Al content) layer placed above the region in the vicinity of a node of the optical standing wave pattern, which is later oxidized to AlOx from the side of the mesa by hot water vapor. The oxide provides good electrical insulation, so that current can flow only through the non-oxidized central region, the so-called "oxide aperture". At the same time, the low refractive index of AlOx (about 1.6) provides an optical confinement, which enables sub-mA threshold currents in standard VCSELs. From the optical point of view, positioning the oxide above or below the cavity is equivalent. But from the electrical standpoint the difference is huge, as can be seen in Fig. 7, which reports the overall operation performance (left) and the current vector maps at 1 mA injection (right). Moving the oxide from the standard configuration to the bottom of the active region almost disables lasing operation, resulting in a much higher threshold current, causing the roll-over optical power to drop from 6 mW to 1 mW. These numerical simulations suggest that the physical interpretation of this effect may be traced back to the asymmetry in the mobilities of the carriers, which should ideally injected in the region centered around the optical field peak. VENUS allows to investigate possible advantages introduced by a double oxide geometry. In the special case of a surface-relief device, VENUS predicts a slightly lower threshold current due to the doubled transverse optical confinement, but also an earlier roll-over. This
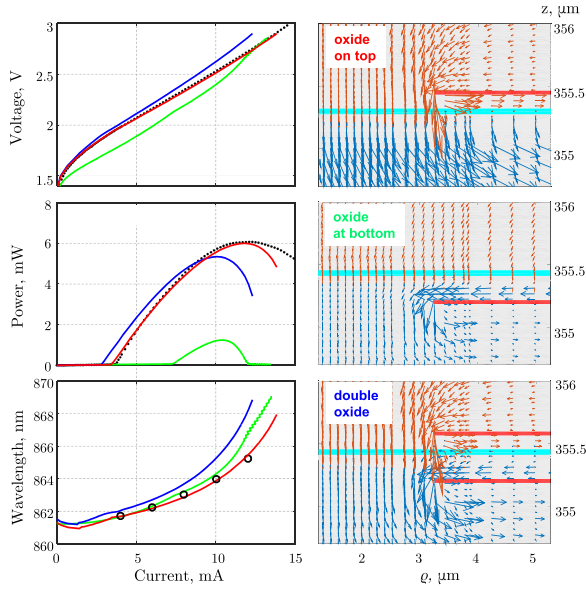
Fig. 7. Left: $V(I)$ (top), $L(I)$ (center) and $\lambda(I)$ (bottom) characteristics. The red, blue and green curves refer to the standard, double and top oxide configurations, respectively. Right: vector plots of the electron (blue) and hole (red) current densities in the device for 1 mA injection; the horizontal red and cyan segments indicate oxide layers and active region, respectively.
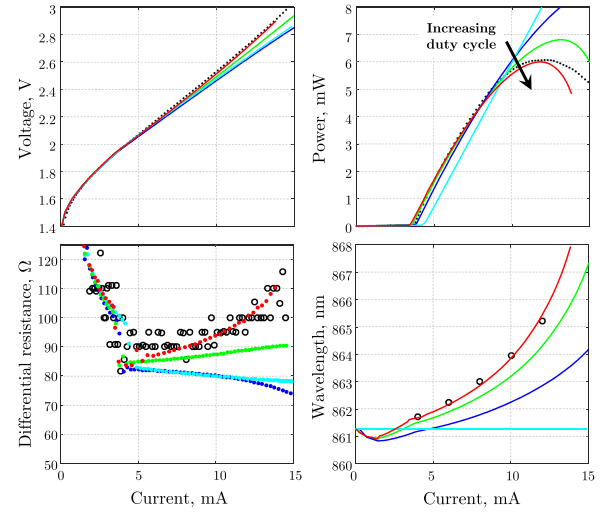

Fig. 8. $V(I)$ (top left) and $L(I)$ (top right) characteristics, differential resistance (bottom left) and lasing wavelength (bottom right) resulting from a simulation campaign investigating pulsed operation. The CW simulations are reported in red, whereas green and blue refer to 80% and 50% pulse duty cycle, respectively. The cyan curves are obtained for constant temperature, corresponding to very short pulses. Open circles indicate experiments.

is caused by the higher heating associated to the more focused current distribution, as can be seen from the steeper wavelength red-shift versus current.

D. Results Under Pulsed Operation

All previous simulations refer to continuous-wave (CW) operation. If the VCSEL is driven in pulsed mode, the heating sources scale almost as the pulse duty cycle. In this view, the pulsed VCSEL performance is investigated by means of a parametric study versus this scaling factor in Fig. 8. In the extreme case of negligible heating, the optical power does no longer exhibit any roll-over (it increases linearly), and the corresponding emission wavelength remains constant. These results show at a glance how heating rules VCSEL operation. In particular, the differential resistance increases due to the thermally induced mobility drop. The resistance increase is a peculiar feature of surface relief devices, as it depends on the device details; in other devices, one observes the opposite trend. It should be pointed out that, for low pulse duty cycles, the increased threshold currents is caused by reduced thermal lensing effects.

IV. CONCLUSIONS

This paper presents our electro-opto-thermal multiphysics simulator VENUS by introducing its main building blocks: optical (VELM), QW optical response, thermal (MEM solver), and electrical (quantum-corrected drift-diffusion). Thanks to the adopted simulation strategy, VENUS can compute light–current–voltage characteristics of a VCSEL in less than one hour on a standard personal computer. VENUS has been applied to the demanding case of a single-mode surface-relief 850 nm

VCSEL and proves to correctly reproduce the experimental results. Observed features can be explained consistently.

Several numerical experiments are discussed. We proved that including the whole substrate leads to a much better agreement with the experimental results. A single oxide aperture positioned just above the active region is shown to be the preferred choice and VENUS can quantify the drawbacks of alternative geometries. The fundamental role of the temperature is clearly demonstrated by mimicking a pulsed operation regime. To the best of our knowledge, this is the first work reporting, based on physics-oriented simulations, the description of these phenomena. This has been possible because VENUS is a completely in-house developed simulator, giving full access to all its components.

VENUS is now ready to be applied to new challenging structures and/or materials, and to be used as a design and optimization tool replacing to the inefficient trial-and-error prototyping approach. Future works will deal with the simulation of non-circular geometries and of the VCSEL dynamic and noise properties.

APPENDIX A
MATERIAL PARAMETERS OF $AL_x GA_{1-x} AS$

This appendix provides some details about the material parameters used in the simulations presented in this work.

The bandgap thermal dependence is modeled as

$$E_g = E_{g,0} - \alpha_g \frac{T^2}{\beta_g + T}. \tag{20}$$

Starting from this expression, the densities of states are evaluated by a many-valley description [59].

TABLE I
TRANSPORT, THERMAL AND OPTICAL PARAMETERS OF AL_x GA_{1-x} AS

Parameter	Values	Ref.
$\varepsilon_{r,s}$	$12.90 - 2.84x$	[62]
$E_{g0,\Gamma}$, eV	$1.519 + 1.115x + 0.37x^2$	[62]
$E_{g0,X}$, eV	$1.981 + 0.124x + 0.144x^2$	[62]
$E_{g0,L}$, eV	$1.815 + 0.69x$	[62]
χ_0, $x < 0.45$, eV	$4.07 - 1.1x$	[62]
χ_0, $x \geq 0.45$, eV	$3.64 - 0.14x$	[62]
β_g, K	204	[62]
α_Γ, eV/K	5.41×10^{-4}	[62]
α_X, eV/K	4.6×10^{-4}	[62]
α_L, eV/K	6.05×10^{-4}	[62]
α_χ, eV/K	2.75×10^{-4}	[62]
ΔE_A, eV	26×10^{-3}	[70]
ΔE_D, eV	5×10^{-3}	[70]
m_Γ/m_0	$0.067 + 0.083x$	[71]
m_X/m_0	$0.850 - 0.140x$	[71]
m_L/m_0	$0.560 + 0.100x$	[71]
m_p/m_0	$0.5 + 0.29x$	[33]
$\mu_{n,300}$, $x < 0.45$, cm^2/s/V	$(8 - 22x + 10x^2) \times 10^3$	[62]
$\mu_{n,300}$, $x \geq 0.45$, cm^2/s/V	$-255 + 1160x - 720x^2$	[62]
$\beta_{\mu,n}$	1	fit
$\beta_{\mu,p}$	1	fit
$\mu_{p,300}$, cm^2/s/V	$370 - 970x + 740x^2$	[62]
$\tau_{n,300}^{SRH}$, ns	5	[62]
$\tau_{p,300}^{SRH}$, ns	20	[62]
β_{SRH}	1	fit
B^{rad}, cm^3/s	1.8×10^{-10}	[62]
C_n^{Aug}, cm^6/s	2.5×10^{-30}	fit
C_p^{Aug}, cm^6/s	10^{-29}	fit
κ_{air}, W/m/K	0.025	[62]
κ_{cavity}, W/m/K	7.8	fit
$\kappa_{mirror,t}$, W/m/K	11.6	fit
$\kappa_{mirror,z}$, W/m/K	9.3	fit
$\kappa_{substrate}$, W/m/K	27.6	fit
κ_{passiv}, W/m/K	0.4	fit
κ_{metal}, W/m/K	300	[62]
β_T	1.30	[62]
n_{AlGaAs}		[72]
$\frac{dn}{dT}$, 1/K	2.8	fit
$\tau_{scat,n}$, ps	2	[62]
$\tau_{scat,p}$, ps	1	[62]

The mobility dependence on doping impurity concentrations is described by the Hilsum model [69]

$$\mu_{n/p,300} = \frac{\mu_{n/p,int}}{1 + \sqrt{\frac{N_A + N_D}{N_X}}}, \qquad (21)$$

where $\mu_{n/p,int}$ indicates the mobility of the intrinsic material, N_D and N_A are the donor and acceptor doping concentrations, and N_X is a fitting parameter; in our simulations, $N_X = 10^{19}$ cm^{-3}.

The thermal dependence of mobility is described by the following expression:

$$\mu_{n/p} = \mu_{n/p,300} \left(\frac{T}{300\,K}\right)^{-\beta_{\mu,n/p}}. \qquad (22)$$

The SRH lifetimes exhibit a similar temperature dependence:

$$\tau_{n/p}^{SRH} = \tau_{n/p,300} \left(\frac{T}{300\,K}\right)^{-\beta_{SRH}}. \qquad (23)$$

APPENDIX B
IMPLEMENTATION DETAILS OF THE SIMULATOR

The results presented in this work have been obtained by means of a MATLAB implementation of VENUS. A typical VENUS simulation yielding one light–current–voltage characteristic (and modal data) with 100 voltage steps takes around 90 minutes on a year 2012 personal computed equipped with a 4-core Intel i7-2600 processor.

Before the multiphysics coupling, each of the VENUS constituents has been validated through comparisons with experimental and/or theoretical results. The optical solver VELM described in Section II-A has been successfully applied to several devices, see, *e.g.*, [23], [61], [73]. The simulator of the quantum well active region discussed in Section II-B has been compared to a genuine quantum-kinetic simulator based on the nonequilibrium Green's function approach, as shown for example in [74]. The heat equation solver described in Section II-C has been validated with the one adopted in [13], where good agreement has been achieved with a numerical complexity reduced by almost a factor of 10, thanks to the spectral element method. Since to the best of our knowledge no similar *quantum-corrected* drift-diffusion software is commercially available, we validated our code without any quantum correction on simple examples (*pin* heterostructures) with Sentaurus Device from Synopsys [18].

The drift-diffusion simulator is the only quasi-3D VENUS component, since the cylindrical symmetry of the VCSEL has been exploited [75]. It is to be remarked that the Scharfetter-Gummel numerical scheme can be extended to three dimensions in a straightforward fashion. However, this is not considered in the present work, as it would blow up the computational cost.

The preliminary step for VENUS simulations is the one-time computation of the optical response look-up table mentioned in Section II-B, which is performed on a HP ProLiant DL560 Gen9 computer with a 10-core parallelization. The Parallel Toolbox exploited in this context is the only additional MATLAB component used in this work. The simulations used in this paper are performed for 30 independent electron and hole densities (900 in total), 24 temperatures (from 290 to 520 K) and 100 wavelength points (from 800 to 900 nm), and require approximately 6 hours. It is to be remarked that this is the only simulation step performed on an ad-hoc computer, even if it could be performed on a standard PC as well.

The physical parameters and the device geometry are introduced in text files containing the same details provided to foundries. These data are used in the optical, electrical, and thermal solvers. The simulation starts with the solution of the Poisson-Fermi equation at thermodynamic equilibrium, to provide a first guess to the quantum-corrected drift-diffusion solver at 0 V. Then, VELM is launched in cold-cavity conditions to initialize all the relevant optical parameters. After this initialization, the drift-diffusion voltage sweep is performed. At the beginning of each cycle the heat/optical solvers are launched,

with the parameters obtained at the end of the previous voltage step. Evaluating the QW optical response requires two steps: first, the 4D look-up table data is interpolated and linearized at the previous voltage. Then, the drift-diffusion model (10) is solved self-consistently by means of Newton's method, using the aforementioned solver outputs as inputs, while gain and spontaneous emission are evaluated efficiently by the linearization of the look-up table.

Since the interplay between electrical and optical/thermal simulators is included only at the end of each voltage step, the electric, optical, and thermal simulations are not solved in a strictly self-consistent fashion. However, this approach is nearly exact when the voltage increment is sufficiently small. While before appreciable current flows, a 200 mV step is appropriate, describing lasing operation and the consequent self-heating accurately requires steps not exceeding 20 mV.

Thanks to its in-house nature it is very simple to schedule parametric simulation campaigns with VENUS such as those presented in this paper. Moreover, we have the full access to a plethora of intermediate results, which represent an important help to grasp the physics behind VCSEL operation.

REFERENCES

[1] R. Michalzik, Ed., *VCSELs: Fundamentals, Technology and Applications of Vertical-Cavity Surface-Emitting Lasers*. Berlin, Germany: Springer-Verlag, 2013.

[2] H. Moench *et al.*, "VCSEL based sensors for distance and velocity," *Proc. SPIE* vol. 9766, Mar. 2016, Art. no. 97 660A.

[3] K. J. Ebeling, R. Michalzik, and H. Moench, "Vertical-cavity surface-emitting laser technology applications with focus on sensors and three-dimensional imaging," *Japanese J. Appl. Phys.*, vol. 52, 2018, Art. no. 08PA02.

[4] C. Gierl *et al.*, "Surface micromachined tunable 1.55 μm-VCSEL with 102 nm continuous single-mode tuning," *Opt. Express*, vol. 19, no. 18, pp. 17 336–17 343, Aug. 2011.

[5] D. D. John *et al.*, "Wideband electrically pumped 1050-nm MEMS-tunable VCSEL for ophtalmic imaging," *J. Lightw. Technol.*, vol. 33, no. 16, pp. 3461–3468, Aug. 2015.

[6] A. Tibaldi, P. Debernardi, and R. Orta, "High-contrast grating performance issues in tunable VCSELs," *IEEE J. Quantum Electron.*, vol. 51, no. 12, 2015, Art. no. 2400407.

[7] G. K. Veerabathran, S. Sprengel, A. Andrejew, and M.-C. Amann, "Room-temperature vertical-cavity surface-emitting lasers at 4 μm with GaSb-based type-II quantum wells," *Appl. Phys. Lett.*, vol. 110, 2017, Art. no. 071 104.

[8] M. Kuramoto *et al.*, "Enhancement of slope efficiency and output power in GaN-based vertical-cavity surface-emitting lasers with a SiO$_2$-buried lateral index guide," *Appl. Phys. Lett.*, vol. 12, 2018, Art. no. 111104.

[9] G. R. Hadley *et al.*, "Comprehensive numerical modeling of vertical-cavity surface-emitting lasers," *IEEE J. Quantum Electron.*, vol. 32, no. 4, pp. 607–616, Apr. 1996.

[10] O. Conradi, S. Helfert, and R. Pregla, "Comprehensive modeling of vertical-cavity laser diodes by the method of lines," *IEEE J. Quantum Electron.*, vol. 37, no. 7, pp. 928–935, Jul. 2001.

[11] J. S. Gustavsson, J. A. Vukusic, J. Bengtsson, and A. Larsson, "A comprehensive model for the modal dynamics of vertical-cavity surface-emitting lasers," *IEEE J. Quantum Electron.*, vol. 38, no. 2, pp. 203–212, Feb. 2002.

[12] P. Nyakas *et al.*, "Self-consistent real three-dimensional simulation of vertical-cavity surface-emitting lasers," *J. Opt. Soc. Amer. B*, vol. 23, no. 9, pp. 1761–1769, 2006.

[13] P. Debernardi, "HOT-VELM: A comprehensive and efficient code for fully vectorial and 3-D hot-cavity VCSEL simulation," *IEEE J. Quantum Electron.*, vol. 45, no. 8, pp. 979–992, Aug. 2009.

[14] R. Sarzala *et al.*, "Numerical self-consistent analysis of VCSELs," *Adv. Opt. Technologies*, vol. 2012, 2012, Art. no. 689 519.

[15] M. Streiff, A. Witzig, M. Pfeiffer, P. Royo, and W. Fichtner, "A comprehensive VCSEL device simulator," *IEEE J. Sel. Topics Quantum Electron.*, vol. 9, no. 3, pp. 879–891, May/Jun. 2003.

[16] K. Mehta *et al.*, "Lateral current spreading in III-N ultraviolet vertical-cavity surface-emitting lasers using modulation-doped short period superlattices," *IEEE J. Quantum Electron.*, vol. 54, no. 4, Aug. 2018, Art. no. 2400507.

[17] *ISE TCAD Release 10.0*, Integrated Systems Engineering AG, Zurich, Switzerland, 2004.

[18] *Sentaurus Device User Guide. Version M-2017.09*, Synopsys, Inc., Mountain View, CA, USA, Sep. 2017.

[19] *Crosslight Device Simulation Software. General Manual*, Crosslight Software Inc., Vancouver, BC, Canada, Sep. 2014.

[20] *RSoft LaserMOD User Guide, v2018.03*, Synopsys, Inc., Optical Solutions Group, Ossining, NY, USA, 2018.

[21] G. P. Bava, P. Debernardi, and L. Fratta, "Three-dimensional model for vectorial fields in vertical-cavity surface-emitting lasers," *Phys. Rev. A*, vol. 63, no. 2, 2001, Art. no. 23816.

[22] P. Debernardi and G. P. Bava, "Coupled mode theory: A powerful tool for analyzing complex VCSELs and designing advanced devices features," *IEEE J. Sel. Topics Quantum Electron.*, vol. 9, no. 3, pp. 905–917, May/Jun. 2003.

[23] P. Debernardi, A. Kroner, F. Rinaldi, and R. Michalzik, "Surface relief versus standard VCSELs: A comparison between experimental and hot-cavity model results," *IEEE J. Sel. Topics Quantum Electron.*, vol. 15, no. 3, pp. 828–837, May/Jun. 2009.

[24] P. Bienstman *et al.*, "Comparison of optical VCSEL models on the simulation of oxide-confined devices," *IEEE J. Quantum Electron.*, vol. 37, no. 12, pp. 1618–1631, Dec. 2001.

[25] M. Dems, R. Kotynski, and K. Panajotov, "Planewave admittance method—A novel approach for determining the electromagnetic modes in photonic structures," *Opt. Express*, vol. 13, no. 9, pp. 3196–3207, 2005.

[26] M. Dems, "Modelling of high-contrast grating mirrors. the impact of imperfections on their performance in VCSELs," *Opto-Electron. Rev.*, vol. 19, no. 3, pp. 340–345, 2011.

[27] K. Seeger, *Semiconductor Physics. An Introduction*, 9th ed. Berlin, Germany: Springer-Verlag, 2004.

[28] B. A. Foreman, "Elimination of spurious solutions from eight-band $k \cdot p$ theory," *Phys. Rev. B*, vol. 56, no. 20, pp. R12 748–R12 751, Nov. 1997.

[29] X. Zhou, F. Bertazzi, M. Goano, G. Ghione, and E. Bellotti, "Deriving $k \cdot p$ parameters from full-Brillouin-zone descriptions: A finite-element envelope function model for quantum-confined wurtzite nanostructures," *J. Appl. Phys.*, vol. 116, no. 3, Jul. 2014, Art. no. 033709.

[30] G. Liu and S.-L. Chuang, "Modeling of Sb-based type-II quantum cascade lasers," *Phys. Rev. B*, vol. 65, 2002, Art. no. 165220.

[31] M. Goano *et al.*, "Challenges towards the simulation of GaN-based LEDs beyond the semiclassical framework," *SPIE Photon. West, Phys. Simul. Optoelectron. Devices XXIV*, B. Witzigmann, M. Osiński, and Y. Arakawa, Eds., vol. 9742, Feb. 2016, Art. no. 974202.

[32] D. Ahn and S.-L. Chuang, "Optical gain in a strained-layer quantum-well laser," *IEEE J. Quantum Electron.*, vol. 24, no. 12, pp. 2400–2406, Dec. 1988.

[33] S. L. Chuang, *Physics of Photonic Devices*. Hoboken, NJ, USA: Wiley, 2009.

[34] P.-F. Qiao, S. Mou, and S. L. Chuang, "Electronic band structures and optical properties of type-II superlattice photodetectors with interfacial effect," *Opt. Express*, vol. 20, no. 2, pp. 2319–2334, 2012.

[35] R. W. Martin and H. L. Störmer, "On the low energy tail of the electron-hole drop recombination spectrum," *Solid State Commun.*, vol. 22, pp. 523–526, 1977.

[36] A. Tomita and A. Suzuki, "A new density matrix theory for semiconductor lasers, including non-Markovian intraband relaxation and its application to nonlinear gain," *IEEE J. Quantum Electron.*, vol. 27, no. 6, pp. 1630–1641, Jun. 1991.

[37] E. Malic and A. Knorr, *Graphene and Carbon Nanotubes. Ultrafast Relaxation Dynamics and Optics*. Weinheim, Germany: Wiley-VCH Verlag, 2013.

[38] F. Bertazzi *et al.*, "Electron transport," in *Handbook of Optoelectronic Device Modeling and Simulation*, J. Piprek, Ed. Boca Raton, FL, USA: CRC Press, 2017, ch. 2, pp. 35–80.

[39] C. Canuto, M. Y. Hussaini, A. Quarteroni, and T. A. Zang, *Spectral Methods: Evolution to Complex Geometries and Applications to Fluid Dynamics*, 1st ed. Berlin, Germany: Springer-Verlag, 2007.

[40] A. Tibaldi *et al.*, "Skew incidence plane-wave scattering from 2-D dielectric periodic structures: Analysis by the mortar-element method," *IEEE Trans. Microw. Theory Technol.*, vol. 63, no. 1, pp. 11–19, Jan. 2015.

[41] U. Aeberhard, "Photovoltaics at the mesoscale: Insights from quantumkinetic simulation," *J. Phys. D*, vol. 51, no. 32, 2018, Art. no. 323002.

[42] C. Jacoboni, *Theory of Electron Transport in Semiconductors. A Pathway from Elementary Physics to Nonequilibrium Green Functions*. Berlin, Germany: Springer-Verlag, 2010.

[43] E. Bellotti, F. Bertazzi, S. Shishehchi, M. Matsubara, and M. Goano, "Theory of carriers transport in III-nitride materials: State of the art and future outlook," *IEEE Trans. Electron Devices*, vol. 60, no. 10, pp. 3204–3215, Oct. 2013.

[44] M. Grupen and K. Hess, "Simulation of carrier transport and nonlinearities in quantum-well laser diodes," *IEEE J. Quantum Electron.*, vol. 34, no. 1, pp. 120–140, Jan. 1998.

[45] M. Gioannini, A. P. Cédola, N. Di Santo, F. Bertazzi, and F. Cappelluti, "Simulation of quantum dot solar cells including carrier intersubband dynamics and transport," *IEEE J. Photovolt.*, vol. 3, no. 4, pp. 1271–1278, Oct. 2013.

[46] C. De Santi *et al.*, "Physical mechanisms limiting the performance and the reliability of GaN-based LEDs," in *Nitride Semiconductor Light-Emitting Diodes*, 2nd ed., J. J. Huang, H. C. Kuo, and S.-C. Shen, Eds. Duxford, U.K.: Woodhead Publishing, 2018, ch. 14, pp. 455–489.

[47] M. Goano, "Series expansion of the Fermi-Dirac integral $\mathcal{F}_j(x)$ over the entire domain of real j and x," *Solid-State Electron.*, vol. 36, no. 2, pp. 217–221, 1993.

[48] M. Goano, "Algorithm 745. Computation of the complete and incomplete Fermi-Dirac integral," *ACM Trans. Math. Softw.*, vol. 21, no. 3, pp. 221–232, Sep. 1995.

[49] G. Wachutka, "Consistent treatment of carrier emission and capture kinetics in electrothermal and energy transport models," *Microelectron. J.*, vol. 26, pp. 307–315, 1995.

[50] M. Lades, W. Kaindl, N. Kaminski, E. Niemann, and G. Wachutka, "Dynamics and incomplete ionized dopants and their impact on 4H/6H–SiC devices," *IEEE Trans. Electron Devices*, vol. 46, no. 3, pp. 598–604, Mar. 1999.

[51] R. Heilman and G. Oelgart, "Ionization energy of the carbon acceptor in $Al_x Ga_{1-x}$ As," *Semicond. Sci. Technol.*, vol. 5, pp. 1040–1045, 2015.

[52] M. Vallone, F. Bertazzi, M. Goano, and G. Ghione, "Model for carrier capture time through phonon emission in InGaN/GaN quantum wells," *Phys. Status Solidi B*, vol. 252, no. 5, pp. 971–976, 2015.

[53] M. Vallone, F. Bertazzi, M. Goano, and G. Ghione, "Carrier capture in InGaN/GaN quantum wells: Role of electron-electron scattering," *J. Appl. Phys.*, vol. 121, no. 12, Mar. 2017, Art. no. 123107.

[54] G. Ghione and A. Benvenuti, "Discretization schemes for high-frequency semiconductor device models," *IEEE Trans. Antennas Propag.*, vol. 45, no. 3, pp. 443–456, Mar. 1997.

[55] C. Hirsch, *Numerical Computation of Internal and External Flows*, 2nd ed. Oxford, U.K.: Elsevier, 2007.

[56] D. L. Scharfetter and H. K. Gummel, "Large-signal analysis of a silicon read diode transistor," *IEEE Trans. Electron Devices*, vol. ED-16, no. 1, pp. 64–77, Jan. 1969.

[57] S. Selberherr, *Analysis and Simulation of Semiconductor Devices*. Berlin, Germany: Springer-Verlag, 1984.

[58] H. Martinsson *et al.*, "Transverse mode selection in large-area oxideconfined vertical-cavity surface-emitting lasers using a shallow surface relief," *IEEE Photon. Technol. Lett.*, vol. 11, no. 12, pp. 1536–1538, Dec. 1999.

[59] M. Calciati, A. Tibaldi, F. Bertazzi, M. Goano, and P. Debernardi, "Many-valley electron transport in AlGaAs VCSELs," *Semicond. Sci. Technol.*, vol. 32, no. 5, 2017, Art. no. 055007.

[60] S. Mei and I. Knezevic, "Thermal conductivity of III-V semiconductor superlattices," *J. Appl. Phys.*, vol. 118, 2015, Art. no. 175101.

[61] P. Debernardi, G. P. Bava, C. Degen, I. Fischer, and W. Elsäßer, "Influence of anisotropies on transverse modes in oxide-confined VCSELs," *IEEE J. Quantum Electron.*, vol. 38, no. 1, pp. 73–84, Jan. 2002.

[62] Ioffe Physico-Technical Institute, St. Petersburg, Russia, "Physical properties of semiconductors," [Online]. Available: http://www.ioffe.ru/SVA/NSM/Semicond/index.html

[63] K. D. Chik and B. A. Richardson, "On the origin of the carrier leakage in GaInAsP/InP double heterojunction lasers," *J. Appl. Phys.*, vol. 67, no. 5, pp. 2660–2662, Mar. 1990.

[64] "Auger carrier leakage in III-nitride quantum-well light emitting diodes," *Phys. Status Solidi RRL*, vol. 6, no. 11, pp. 418–420, 2012.

[65] M. Deppner, F. Römer, and B. Witzigmann, "Auger recombination and carrier transport effects in III-nitride quantum well light emitting diodes," *Proc. SPIE* vol. 8619, Mar. 2013, Art. no. 86 191J.

[66] F. Bertazzi, X. Zhou, M. Goano, G. Ghione, and E. Bellotti, "Auger recombination in InGaN/GaN quantum wells. A full-Brillouin-zone study," *Appl. Phys. Lett.*, vol. 103, no. 8, Aug. 2013, Art. no. 081106.

[67] M. Calciati *et al.*, "Correlating electroluminescence characterization and physics-based models of InGaN/GaN LEDs: Pitfalls and open issues," *AIP Adv.*, vol. 4, no. 6, Jun. 2014, Art. no. 067118.

[68] F. Bertazzi *et al.*, "Looking for Auger signatures in III-nitride light emitters: A full-band Monte Carlo perspective," *Appl. Phys. Lett.*, vol. 106, no. 6, Feb. 2015, Art. no. 067118.

[69] C. Hilsum, "Simple empirical relationship between mobility and carrier concentration," *Electron. Lett.*, vol. 10, no. 13, pp. 259–260, 1974.

[70] H. C. Casey, Jr. and M. B. Panish, *Heterostructure Lasers. Part A: Fundamental Principles*. New York, NY, USA: Academic, 1978.

[71] S. Adachi, "GaAs, AlAs, and $Al_x Ga_{1-x}$ As: Material parameters for use in research and device applications," *J. Appl. Phys.*, vol. 58, no. 3, pp. R1–R29, Aug. 1985.

[72] S. W. Corzine, "Design of vertical-cavity surface-emitting lasers with strained and unstrained quantum well active regions," Ph.D. dissertation, Dept. Elect. Commun. Eng., Univ. California, Santa Barbara, Santa Barbara, CA, USA, 1993.

[73] P. Debernardi *et al.*, "Theoretical-experimental study of the vectorial modal properties of polarization-stable multimode grating VCSELs," *IEEE J. Sel. Topics Quantum Electron.*, vol. 13, no. 5, pp. 1340–1348, Sep./Oct. 2007.

[74] A. Tibaldi, J. A. Gonzales Montoya, F. Bertazzi, M. Goano, and P. Debernardi, "Bridging scales in multiphysical VCSEL modeling," in *Proc. 18th Int. Conf. Numer. Simul. Optoelectron. Devices*, Hong Kong, Nov. 2018, pp. 19–20.

[75] M. Spevak and T. Grasser, "Discretization of macroscopic transport equations on non-cartesian coordinate systems," *IEEE Trans. Computer-Aided Des.*, vol. 26, no. 8, pp. 1408–1416, Aug. 2007.

Alberto Tibaldi was born in Casale Monferrato, Italy, in 1987. He received the B.Sc., M.Sc., and Ph.D. degrees in electronic engineering from Politecnico di Torino, Turin, Italy, in 2009, 2011, and 2015, respectively. In 2012, he joined the Italian National Council of Research as a Research Fellow. He currently teaches courses on numerical analysis and semiconductor device simulation. His research interests include electrical and optical modeling of photonic devices.
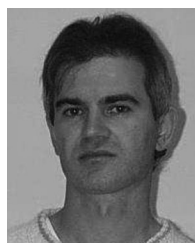
Francesco Bertazzi received the Laurea and Ph.D. degrees in electronics engineering from the Politecnico di Torino, Turin, Italy, in 2000 and 2003, respectively. He was a Visiting Scholar with the Department of Electrical and Computer Engineering, Boston University, Boston, MA, USA. Since 2008, he has been a Professor with the Dipartimento di Elettronica, Politecnico di Torino. His Ph.D. studies were focused on electromagnetic modeling of traveling-wave structures for optoelectronic applications and nonlinear physics-based noise analysis of RF and microwave devices. His research activities at Boston University included material-theory-based modeling of band structures, vibrational properties, and carrier scattering rates, essential for the study of the complex electronic, transport, and optical properties of novel wide-gap semiconductors, in particular III-nitrides and II-VI oxide semiconductors. His present research activity is focused on density matrix and nonequilibrium Green's function modeling of carrier transport and recombination processes in optoelectronic devices (HgCdTe infrared photodetectors, InGaN light-emitting diodes, and VCSELs).

Michele Goano (M'98) received the Laurea and Ph.D. degrees in electronic engineering from Politecnico di Torino, Turin, Italy, in 1989 and 1993, respectively. In 1994 and 1995, he was a Postdoctoral Fellow with the Département de Génie Physique, École Polytechnique de Montréal, Montréal, QC, Canada. He joined the faculty of Politecnico di Torino in 1996. He has been a Visiting Scholar with the School of Electrical and Computer Engineering, Georgia Institute of Technology, Atlanta, GA, USA, with the Department of Information Technology and Media, Mid-Sweden University, Sundsvall, Sweden, and with the Department of Electrical and Computer Engineering, Boston University, Boston, MA, USA. His current research activity is focused on the simulation of optoelectronic devices based on narrow- and wide-bandgap semiconductor materials.

Rainer Michalzik received the Dipl.-Ing. degree in electrical engineering from the Technical University of Braunschweig, Braunschweig, Germany, in 1989, and the Dr.-Ing. and habilitation degrees from Ulm University, Ulm, Germany, in 1996 and 2009, respectively. He was appointed as an Apl. Professor in 2012.

Since 2001, he has been leading the VCSELs and Optical Interconnects Research Group, Institute of Functional Nanosystems (Institute of Optoelectronics until June 30, 2018), Ulm University, Ulm, Germany. He has edited the book entitled *VCSELs — Fundamentals, Technology and Applications of Vertical-Cavity Surface-Emitting Lasers* (Berlin, Germany: Springer, 2013).

Pierluigi Debernardi was born in Casale Monferrato and received the degree in electronics engineering from Politecnico di Torino, Turin, Italy, in 1987. Since 1989, he has been with the Italian National Council of Research. His interests are mainly in the field of the modeling of semiconductor materials and devices for optoelectronic applications. He is currently involved in modeling and designing VCSEL structures with non-circular and/or complex geometries, so as to achieve specific performances.